Review

Zhandong Li and Dmitry Kurouski*

Nanoscale structural characterization of plasmon-driven reactions

Abstract: Illumination of noble metal nanostructures by electromagnetic radiation induces coherent oscillations of conductive electrons on their surfaces. These coherent oscillations of electrons, also known as localized surface plasmon resonances (LSPR), are the underlying physical cause of the electromagnetic enhancement of Raman scattering from analytes located in a close proximity to the metal surface. This physical phenomenon is broadly known as surface-enhanced Raman scattering (SERS). LSPR can decay via direct interband, phonon-assisted intraband, and geometry-assisted transitions forming hot carriers, highly energetic species that are responsible for a large variety of chemical transformations. This review critically discusses the most recent progress in mechanistic elucidation of hot carrier-driven chemistry and catalytic processes at the nanoscale. The review provides a brief description of tip-enhanced Raman spectroscopy (TERS), modern analytical technique that possesses single-molecule sensitivity and angstrom spatial resolution, showing the advantage of this technique for spatiotemporal characterization of plasmon-driven reactions. The review also discusses experimental and theoretical findings that reported novel plasmon-driven reactivity which can be used to catalyze redox, coupling, elimination and scissoring reactions. Lastly, the review discusses the impact of the most recently reported findings on both plasmonic catalysis and TERS imaging.

Keywords: bimetallic nanostructures; hot carriers; monometallic nanostructures; plasmonic catalysis; SERS; TERS.

*Corresponding author: Dmitry Kurouski, Department of Biochemistry and Biophysics, The Institute for Quantum Science and Engineering, Texas A&M University, College Station, TX 77843, USA, E-mail: dkurouski@tamu.edu
Zhandong Li, Department of Biochemistry and Biophysics, Texas A&M University, College Station, TX 77843, USA. https://orcid.org/0000-0002-3333-1880
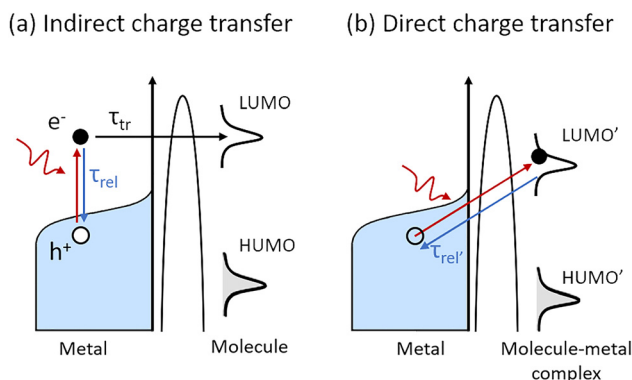
1 Introduction

Noble metal nanostructures absorb light in the visible and infrared (IR) parts of electromagnetic spectrum. Illumination of noble metal nanostructures by electromagnetic radiation induces collective oscillations of conductive electrons on their surfaces [1–6]. Energy of these collective electron oscillations, also known as localized surface plasmon resonances (LSPRs), is determined by the size of nanoparticles, their shape, nature of metal, and dielectric environment [7, 8]. LSPRs are responsible for 100–1000-fold enhancement of the local electric field (E). This yields 10^4–10^8 enhancement of the Raman scattering from molecules located in the close proximity to the metal surfaces [1, 9–11]. Discovered in 1970s, this physical phenomenon has been rapidly grown into a broadly used analytical approach that is known as surface-enhanced Raman spectroscopy (SERS) [12–15]. Single-molecule sensitivity of SERS makes this technique highly useful in numerous areas of applied and fundamental research that spans across forensics, food chemistry, electrochemistry and catalysis [2, 16, 17].

LSPRs can decay via both radiative and nonradiative pathways [18, 19]. Upon a radiative decay, plasmon energy is dissipated through the elastic scattering of photons. Nonradiative decay or Landau damping of LSPRs results in formation of hot carriers through either direct interband, phonon-assisted intraband or geometry-assisted transitions [19–21]. Hot carriers are highly energetic species that persist for a few tens of femtoseconds to picoseconds [22, 23]. They can further decay via electron–electron or electron–phonon scattering, or they can populate unoccupied orbitals in molecules located near metal surfaces [24, 25]. In the latter scenario, hot carriers can be injected into the electronic states of a nearby molecule, inducing a large spectrum of chemical reactions, Figure 1.

These are ongoing discussion about a contribution of plasmonic heating in such processes. Several research groups performed elegant experiments to determine an increase in temperature caused by plasmonic heating in a junction between two nanostructures, also known as a "hot-spot". Using an ultrafast surface-enhanced Raman thermometry technique, Frontiera's group found that upon plasmon excitation,

(a) Indirect charge transfer (b) Direct charge transfer

Figure 1: Mechanisms of hot carrier transfer to molecular analytes. (a) In indirect charge transfer, energetic electron is generated in metal and subsequently transferred to analyte. (b) In direct charge transfer, hot electron is generated directly onto the LUMO of molecule–metal complex in one step.

temperature in the hot-spot increases on the order of tens of kelvin even for extremely high photoexcitation values. This experimental evidence demonstrated that plasmon-driven chemistry observed on SERS platforms (noble metal nanostructures and SERS substrates) is not thermally driven. Large group used finite density time domain (FDTD) calculations to predict changes in temperature in tip-sample junction upon its illumination with red (λ = 671 nm) laser light [26]. The researchers found that a temperature change in the tip-sample junction directly depends on the distance between the tip and the sample. At the same time, FDTD calculations predicted not more than 40 K change in temperature upon illumination of the metalized scanning probe by 500 μW of 671 nm light. These findings are coherent with results of the experimental work recently reported by Richard-Lacroix and Deckert [27]. Measuring Stokes and anti-Stokes vibrations of 16-mercaptohexadodecanoic acid adsorbed to the metal surface, Richard-Lacroix and Deckert found that an average temperature at the tip-sample junction was about 80 °C when 100 μW of 532 nm laser light was used [27]. These theoretical and experimental findings show that observed by TERS plasmon-driven chemistry is attributed to hot carriers rather than an increase in temperature.

2 SERS-based plasmon-driven reactions

2.1 Plasmon-driven redox reactions

There are numerous SERS studies of plasmon-driven reactions [28–31] including hydrogen dissociation [32, 33]

and reduction of 4-nitrobenzenethiol (4-NBT) to DMAB on the single hot-spot [34] and single-molecule [35] levels. An excellent mechanistic study was recently reported by Weng and coauthors in which the researchers showed that the yield of DMAB could be altered by protic solvents, such as water [36]. It has been found that the yield of DMAB could be controlled by 1-octanethiol and poly-vinylpyrrolidone. This suggests that these molecules compete with 4-NBT for the adsorption sites on the metal surface. Kang and coworkers used SERS to determine how rates of 4-NBT to DMAB reduction change under different strengths of the electric field and under different environments [37]. The researchers found that under nitrogen, hydrogen and water atmospheres, an increase in the intensity of the external electric field caused an increase the rate of 4-NBT to DMAB reduction. However, if the reaction took place in an oxygen atmosphere, the opposite relationship was observed between the reaction rate and strength of the electric field. These results suggest that oxygen is far more reactive than 4-NBT. Thus, plasmons generated on monometallic nanostructures are transferred to oxygen rather than to 4-NBT.

Using electrochemical SERS, Tian's group discovered that 4-aminothiophenol (4-ATP) could be oxidized to *p,p'*-dimercaptoazobisbenzene (DMAB) at very negative surface potentials or by illumination of SERS substrate by low-power laser light [38]. This finding was confirmed by a surface mass spectrometry experiment. Such extensive experimental and computational approaches to elucidate the reaction product of plasmon-driven 4-ATP oxidation were used to disprove initial conclusions based on SERS study of 4-ATP: new bands observed in SERS of 4-ATP were incorrectly assigned as non-totally symmetric (b_2) vibrations of 4-ATP [39]. Ren's and Tian's groups also found that plasmon-driven oxidation of 4-ATP occurred only in the presence of molecular oxygen [40]. The researchers proposed that oxygen molecules are first activated by hot carriers which results in formation of oxygen anions, species that perform the two-electron oxidation reaction of 4-ATP.

Van Duyne's group monitored redox chemistry of ferri- and ferro-hexacyanide complexes ([Fe (III)(CN)$_6$]$^{3-}$/[Fe (II)(CN)$_6$]$^{4-}$ [Fe-(III)/Fe (II))], Figure 2 [41]. These complexes are the ideal model for elucidation of such plasmon-driven redox chemical reactions because of their hot-electron [42] and hot-hole chemistry [43]. Qi and co-workers used AuNPs-based SERS to monitor a two-step transformation between Fe (III) and Fe (II) ions. It has been found that the transformation is triggered by plasmon-driven charge transfer process in which femtosecond time scale hot
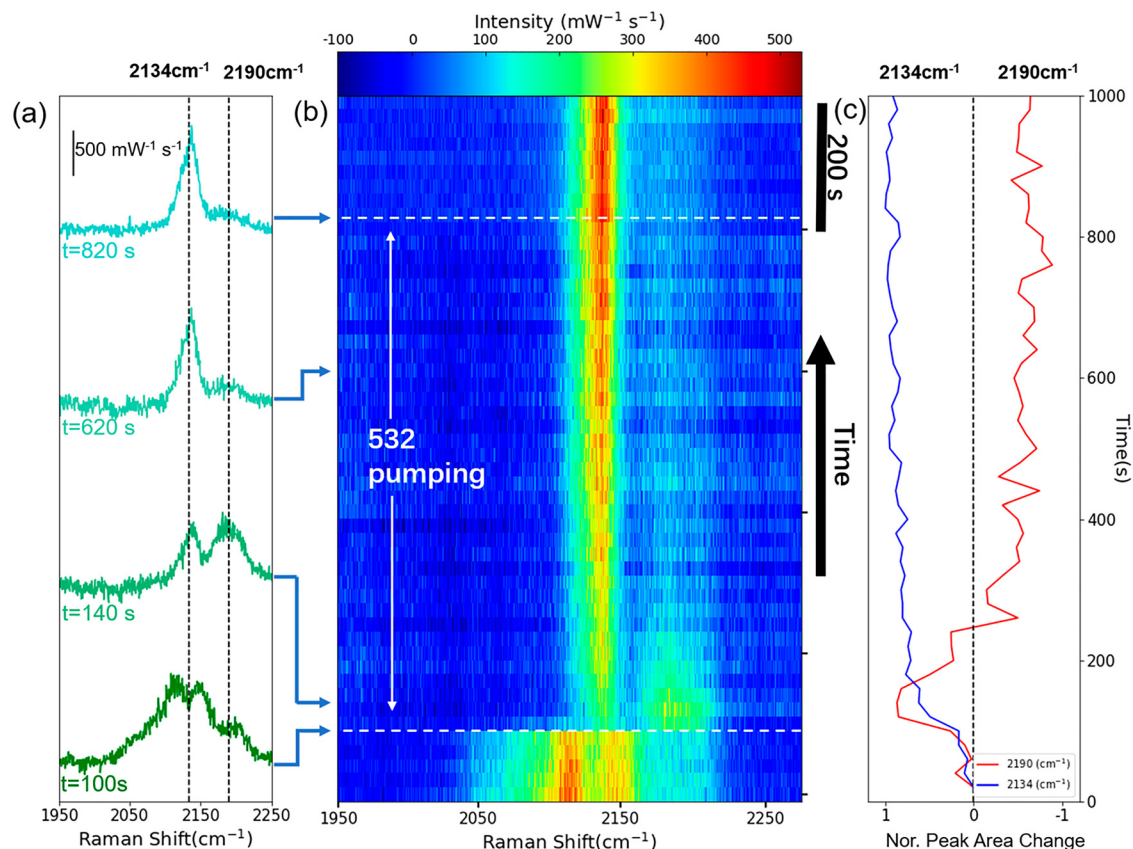
Figure 2: In situ spectrum of ferri/ferrocyanide reaction on AuNPs.
(a) SERS spectra at different time points ranging from 100, 140, 620 to 820 s. (b) Stacking of SERS spectra with time at 785 nm laser beam, spectral changes were observed after the 532 nm optical pumping was turned on. (c) Peak area changes with time of bands at 2190 and 2134 cm^{-1} [41].

electron and hot hole transfer occurred competitively under 532 nm illumination. This led to significantly slower macroscopic accumulation of the oxidized species and the slow chemical dynamics observed in this plasmon-induced charge transfer process.

In addition to the aforementioned 4-NTP and 4-ATP to DMAB reduction [38–40], plasmons can be used to catalyze Suzuki-Miyaura coupling reaction [44]. Chen's group used SERS to investigate mechanism of a PdNP-catalyzed Suzuki–Miyaura cross-coupling reaction, Figure 3 [45]. The researchers found that the particle charge and the surface ligands could affect the molecule-Pd interactions that were critically important for such coupling reaction. It has been also found that soluble Pd species were not catalytically active because they were not in a direct contact with the aryl halides. This evidence suggested that catalytic activity of plasmonic systems can enhanced by modification of the surface ligand and by modification of interactions between the reactant and the nanostructure.

2.2 Plasmon-driven scissoring and elimination reactions

There are several plasmon-driven scissoring reactions including cleavage of carbon–carbon (C–C) [46], nitrogen–nitrogen (N=N) [47] and gold–sulfur (Au–S) [26] bonds, as well as dissociation of H_2 and O_2 that are caused by scissoring of H–H [48] and O–O [49] bonds respectively. Sun and coworkers showed that under acidic conditions, DMAB could be cleaved by hot carriers producing two molecules of 4-ATP, Figure 4. However, under alkaline conditions, DMAB scissoring yields two molecules of 4-NBT instead of 4-ATP [47]. Using SERS, Huh and coworkers demonstrated thiophenol as a yield from both 4-mercaptobenzoic acid (4-MBA) and 4-mercaptobenzyl alcohol (4-MBM), Figure 4 [46]. Their findings suggested that plasmon-driven decarboxylation of 4-MBA was much more efficient when the carboxyl group of 4-MBA was deprotonated. Interestingly, plasmon scissoring was not observed if the carboxyl group of 4-MBA has been esterified. Huh and coworkers also
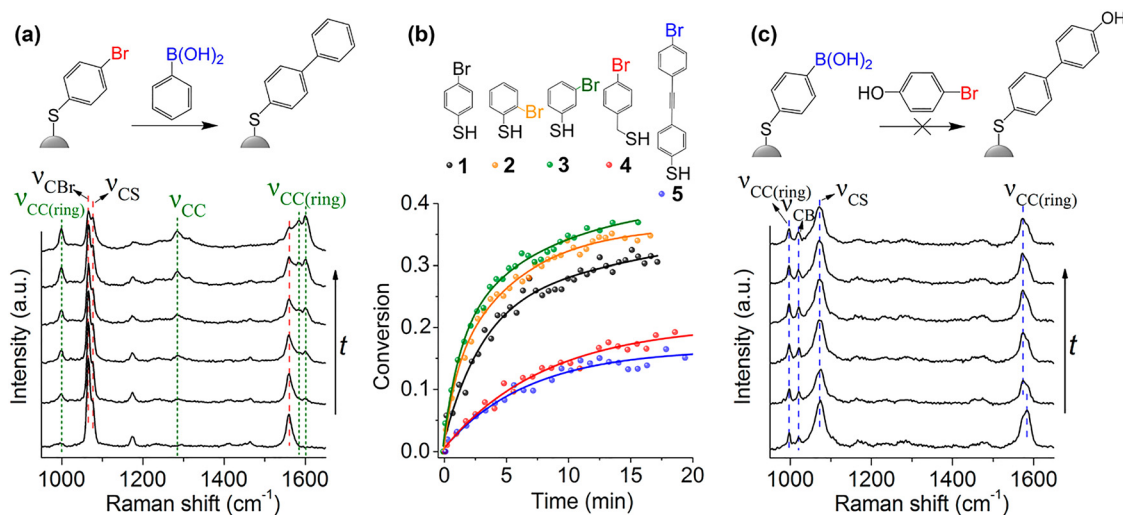
Figure 3: Suzuki-Miyaura reactions monitored by SERS.
(a) SER spectra of Suzuki-Miyaura reactions at different time points on 4-BTP coated Au-Pd structures. (b) Kinetics of the reaction with different precursors. (c) SER spectra of 4-mercapto-phenylboronic acid (4-MPBA) on Au-Pd structures [45].
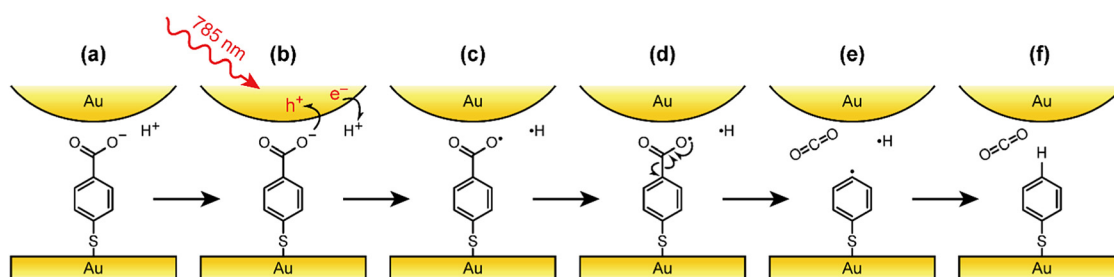

Figure 4: Mechanism of the plasmon-driven scissoring reaction proposed by Yoon group.
Hot holes from Au-coated tip are transferred to carboxylate anion of 4-MBA (a-b), while hot electrons are transferred to protons, leading to the formation of carboxyl radicals and hydrogen atoms (c-d). The radicals then undergo intermolecular rearrangement that leads to the C-C bond cleavage (e-f) [46].

performed an elegant experiment in which they tested the impact of oxygen on the observed C–C bond scissoring of MBA. The presence of oxygen was found to be critically important for the observed C–C bond cleavage. These findings resonate with the conclusions of the Ren's and Tian's groups regarding plasmon-driven oxidation of 4-ATP [39, 40]. Based on these findings, one can hypothesize that plasmon-driven activation of oxygen, rather than molecular analytes, can be the first step in plasmon-driven chemical reactions.

An activation of the carbon-halogen (C–X) bond that leads to elimination of halogen is very important chemical reactions used in organic synthesis. Tian's group used 8-bromoadenine (8BrAd) as a molecular reporter to study the effect of the electrode potential, laser wavelength, and power on plasmon-mediated chemical reactions (PMCR) kinetics on AgNP-modified silver electrodes [50]. The researchers combined both experimental methods (in situ electrochemical SERS) and theory (DFT calculation) to investigate the plasmonic-driven cleavage of C–Br bond in 8BrAd, Figure 5. The results indicated that the energy level of the hot electrons generated from plasmonic relaxation can be controlled by applied potentials and laser light. They propose the mechanism of modulating matched energy of plasmon relaxation-generated hot electrons will help promote the efficiency of plasmon-induced reactions in electrochemical interfaces. These findings can be used to facilitate the control of PMCR on nanostructures. These findings suggest a new strategy for plasmon-drive halogen elimination on plasmonic nanoparticles that can be used in organic synthesis.

Interesting hot carrier reactivity was reported by Zhang and coworkers [51] that leads to NO_2 elimination (C–N dissociation) in 4-nitrobenzenethiol, as well as by Schürmann and Bald [52] reported C–Br cleavage in bromoadenine. Extensive analysis of hot carrier-driven reactions discovered using SERS can be found in excellent reviews by Kim [53, 54], Linic [55, 56], Halas [57], Schlücker [28] and Maier [25].
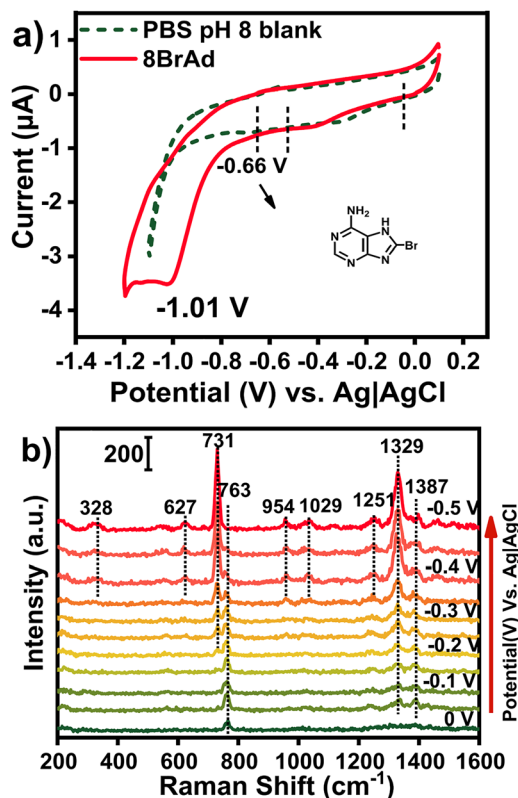
Figure 5: (a) Cyclic-voltage curves of silver nanoparticles @ silver electrode in the presence (red line) and absence (dotted green line) of 8-BrAd. (b) EC-SERS of 8BrAd on AgNPs@Ag electrode (532 nm laser @ 0.1 mW) [50].

Figure 6: Experimental set-up of nanophotonic chip that can be used to enhance plasmon-driven catalysis.
(a) Au@Ag nanoparticles are embedded into a dielectric photonic crystal to form the plasmonic/photonic hybrids. (b) Simulated absorption σ_{abs} of single Au@Ag on the photonic crystal surface. (c) Hot-electron-driven reduction of 4-NTP to 4-ATP [60].

3 Methods for enhancement of plasmon-driven reactivity

3.1 Synthetic approaches for the enhancement of hot carrier-driven reactivity

Plasmonic photocatalysis has been emerged as a potential method for achieving high efficiency and selectivity [58]. Many reactions such as the molecular desorption, redox and scissoring reactions can take place on the interface of plasmonic nanostructures [59]. This opens up a possibility to modulate such reactivity by changing the strength of the electric field, laser wavelength and by modifications of nanoparticles. Cunningham's group develops a plasmonic–photonic resonance hybridization method that allowed for significant enhancement of generation of hot electron at tunable, narrow-band wavelengths[60]. The researchers have coupled the plasmon resonance of Ag nanoparticles to the guided mode resonance in a dielectric photonic crystal slab where the hot-electron triggered
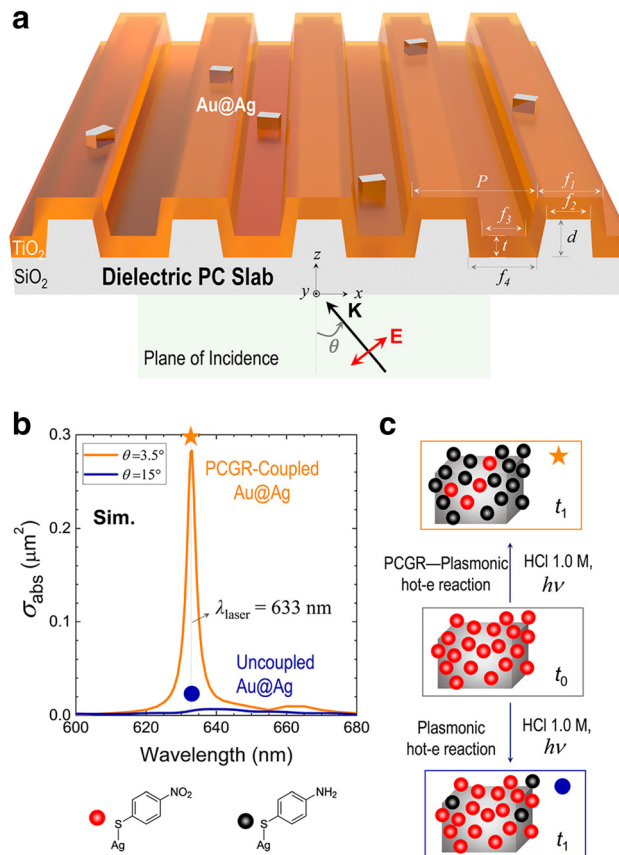
reduction is significantly enhanced at selected narrowband wavelengths and broad spectral tunability, Figure 6. The generation of more hot electron was achieved by coupling plasmonic NPs to a photonic microcavity resonator and form an intense optical hotspot at the nanoparticle so that the LSPR and on-resonant photonic crystal guided resonance (PCGR) hybridization will enhances the hot carrier generation significantly at selected narrowband wavelengths while simultaneously possessing broad spectral tunability. This method has been tested to be suitable and compatible for several nanoparticles which facilitate the controlling of corresponding optical-chemical properties.

Wang's group proposed to use the piezotronic effect to enhance plasmonic photocatalysis on AuNPs/BaTiO$_3$ heterostructures, Figure 7 [61]. The researchers prepared Au$_x$/BaTiO$_3$ plasmonic photocatalysts by precipitating AuNPs on piezoelectric BaTiO$_3$ nanocubes through a chemical method. To investigate the piezoelectric effect of BaTiO$_3$ nanocubes, simulations of the piezopotential are required. There is local
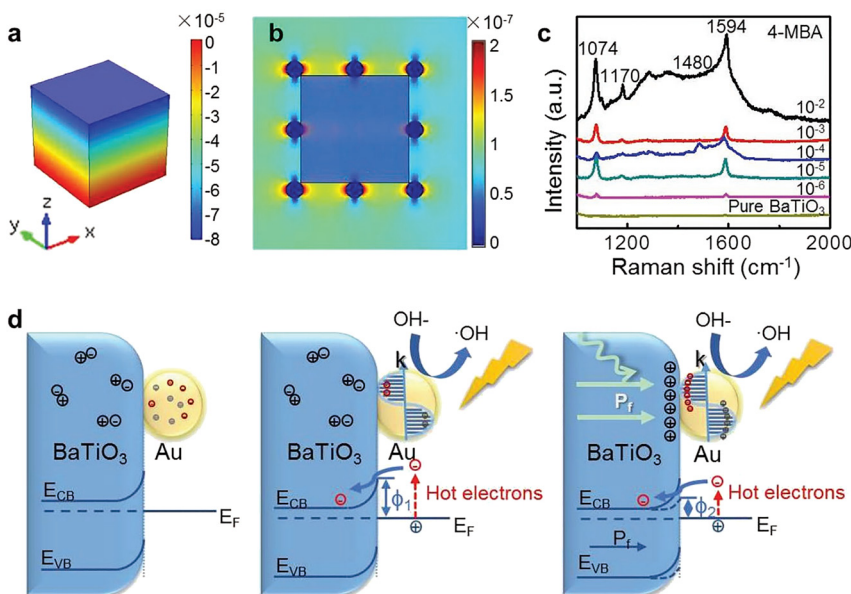
Figure 7: (a) 3D Simulation of the piezoelectric effect in BaTiO₃ nanocube. (b) Electric field distribution on gold nanoparticles on BaTiO₃ NC showing the enhancement. (c) SERS of 4-mercaptobenzoic acid on the Au-BaTiO₃ complex. (d) Mechanism of the piezotronics-enhanced photocatalysis [61].

high pressure caused by the cavitation bubbles during the instantaneous collapse of bubbles which will induce significant piezopotential in single piezopotential in the adjacent $BaTiO_3$ single crystals. Therefore, $BaTiO_3$ nanocubes with 100 nm of length and width are chosen for theoretical simulations where the piezopotential distribution is performed under sonication and 10 MPa pressure simulated environment, as shown in Figure 7a. It was proved by the theoretical results that sonication can cause high piezopolarization across the nanocrystal with only 100 nm size. The deformation of $BaTiO_3$ results in the generation of the piezoelectric field, leading to further separation of photon-generated electrons and help improving production of hydroxyl radicals. The mechanism of this elevated sonic-photocatalysis by $Au_x/BaTiO_3$ can be explained by schematic in Figure 7. In the complex of Au and $BaTiO_3$, Au nanoparticle was partially embedded in $BaTiO_3$ nanoparticle (Figure 7d) where $BaTiO_3$ nanoparticle have some defect on the surface of the crystal as a wide bandgap semiconductor. When these two types of particles contact (Figure 7d left), the charges will redistribute at the complex because of their different Fermi level, as a result of the electrons transfers from $BaTiO_3$ nanoparticle to AuNP so that the Schottky barrier is formed at their interface. When the complex was excited by all spectrum light (Figure 7d middle), Au nanoparticles show LSPR and decay into hot electrons, which will transfer across the Schottky barrier to $BaTiO_3$ nanoparticles and the leave holes being further captured by the donors, resulting in the oxidation reactions of MO. In addition, under the sonication-induced pressure on $BaTiO_3$, there will be a built-in piezoelectric field inside $BaTiO_3$ nanocubes (Figure 7d right), which helps suppress the recombination of hot electron-hole and forced more excited

holes in the interface of the complex leading to more oxidation of MO by the increased radicals.

3.2 Role of metal and nanoparticle shape in plasmon-driven catalysis

A nature of metal, morphology and shape of nanoparticles are of significant importance for the light–matter interactions and, consequently, plasmonic/catalytic performance. Halas' group reported the photocatalytic activities of a series of aluminum nanoparticles including nanocubes, octopods and nanocrystals and summarizes the corresponding shape dependence [62]. These particles exhibit very similar LSPRs to noble metal nanostructures. Halas' group found that the octopods exhibited 10-fold higher reaction rate than the nanocrystals and five folds higher than nanocubes, with 45 and 49% lower apparent activation energy than nanocubes or nanocrystals, respectively, Figure 8.

3.3 Plasmon-driven reactions on bimetallic nanostructures

The catalytic properties of noble metal nanostructures can be broadened by coupling noble with catalytic metals such as palladium (Pd), ruthenium (Ru) or platinum (Pt) in one bimetallic construct [63]. Such bimetallic nanostructures catalyze a broad range of chemical reactions. In this case, catalytic efficiency and selectivity of bimetallic nanostructures directly depends on the choice of the catalytic metal. For example, Wang and coworkers showed that
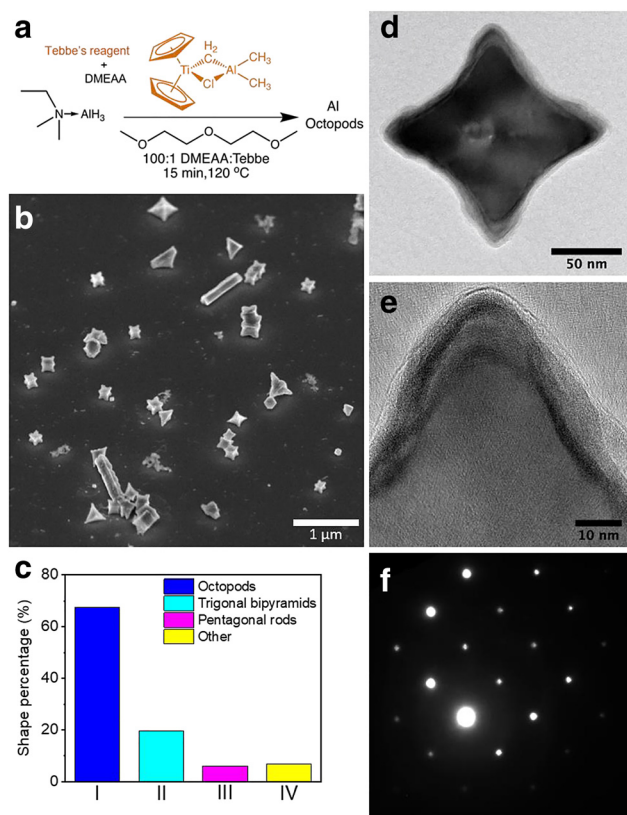
Figure 8: Preparation of aluminum octopod and high-resolution TEM.
(a) Schematic illustration of the preparation process of aluminum octopod. (b) Tilted (45°) SEM of the morphology in aluminum octopods solution. (c) Statistical of the percentage of different shapes of aluminum nanoparticles. (d) High-resolution TEM of aluminum octopod. (e) Zoom-in inspection of the corner of Al octopods. (f) SAED of the selected aluminum octopods [62].

gold–palladium (Au@Pd) nanoparticles performed a plasmon-enhanced Suzuki coupling reaction [64]. They reported a twofold increase in the reaction rate and yield using Au@Pd nanostructures when compared to the rate and yield of corresponding monometallic nanostructures. Halas' group showed that cupper ruthenium (Cu@Ru) nanostructures could be used for light-driven dry reforming of methane with carbon dioxide, a reaction that yields a syngas [65]. It should be noted that such reforming could not be performed on the monometallic counterparts of Cu@Ru or on Au@Pd nanostructures. Lou et al. found that platinum–gold nanoprisms were capable of hydrogen generation [66]. They investigated several different classes of platinum–gold nanoprisms, including Pt-covered, Pt-edged and Pt-tipped Au nanoprisms [66]. They found that Pt-edged bimetallic nanostructures exhibited nearly five times more efficient hydrogen generation than Pt-covered and Pt-tipped platinum–gold nanoprisms. These findings suggest that the catalytic efficiency of bimetallic nanostructures also depends on nanoscale structural organization, which remains poorly understood.

4 Spatiotemporal characterization of hot carrier-driven reactions

4.1 Tip-enhanced Raman spectroscopy (TERS)

Although SERS allows for quantitative analysis of the reaction products and their precise chemical analysis, this analytical technique lacks spatial resolution that is often required to reveal the origin of significant variability of catalytic efficiency on both mono- and bimetallic nanostructures.

Tip-enhanced Raman spectroscopy allow for overcoming these limitations. In TERS, noble metal nanostructure is formed at the apex of the scanning probe either by electrochemical etching of gold (Au) or silver (Ag) wire in the case of STM-based TERS (STM-TERS) [67, 68]. Alternatively, such nanostructures can be created by deposition of noble metals on commercially available silicon or silicon nitride scanning probes. Such plasmonic probes are typically used in AFM-based TERS (AFM-TERS) [69, 70]. After such plasmonic probe is positioned above a sample of interest, it is illuminated by electromagnetic radiation in either bottom-, side- or top or configuration geometrics. The first two optical configurations are typically used for TERS imaging of opaque samples. Bottom or epi configuration is ideal for TERS imaging of transparent or translucent samples. Excellent light collection efficiency that can be achieved by oil-immersed objectives for illumination of the probe and collection of scattering photons allows for maximization of signal-to-noise ratio in collected TERS spectra [71–74]. Lastly, a parabolic mirror can be used to enable optical access to the scanning probe [30]. Although in theory such focusing geometry allows for highly efficient light collection, parabolic mirror-based experimental setups did not gain much popularity due to higher complexity for alignment and focusing.

TERS provides subnanometer spatial resolution [75, 76], which can be used to unravel secondary structure of protein aggregates [77–79], composition of cell membranes [80, 81], molecule-substrate interactions [68, 82, 83], as well as elucidate electrochemical [69, 84–88] and photocatalytic processes [34, 89, 90] at the nanoscale. The image is adopted from the review by Kurouski et al. [91].

4.2 Plasmonic reactions on mono- and bimetallic nanoparticles

Our group discovered that the edges of Au nanoplates (AuNPs) exhibited much higher plasmon-driven oxidation activity comparing to the center of these nanoplates (Figure 9) [89]. Similar conclusions were made based on TERS imaging of 4-NBT reduction to DMAB on AuNPs and Au microplates (AuMPs) [89, 90]. El-Khoury's group employed TERS to probe spatial variations in intensities of optical fields on the surface of Ag nanoparticles (AgNPs) and Ag nanowires (AgNWs) [92, 93]. The electric field was found to be higher at the edges and corners of these AgNPs and AgNWs comparing to their terraces [94, 95]. These finding suggests that the strength of the electric field can determine catalytic activity of nanostructures. To test this hypothesis, our group used TERS to measure the reaction rates for 4-NBT conversion to DMAB on AuNPs [90]. We found that an increase in the electric field, which can be achieved by an increase in power of the incident laser light, led to an increase in the reaction rate of 4-NBT to DMAB reduction.

Using 3D TERS, our group investigated the relationship between metal crystal facets and catalytic activity [96]. The 3D TERS effect arises from localization of plasmonically active zones of the shaft of the scanning probes. TERS signal provided by such zones allows for structural characterization of sides of the analyzes specimens. It should be noted that the nanostructure located at the apex of the shaft-active scanning probes can be used to probe the top surfaces of analyzed samples. In the first proof-of-principle experiment, 3D TERS was used to determine catalytic activity of Au microplates (AuMPs) that had 40–100 nm in height and stretched for microns in length. Wand and Kurouski found that the top surface AuMPs had Au{111} facets, whereas sides had Au{110} or {100} crystal facets. Next, the researchers formed a monolayer of 4-NBT on AuMPs and chemically reduced it using sodium borohydride. 3D TERS revealed that Au{111} facet exhibited much higher efficiency in chemical reduction of 4-NBT to DMAB than Au Au{110} or {100}. It should be noted that metal crystal facets exhibit different catalytic activity in chemical and plasmon-driven reactions. Specifically, Rossi and
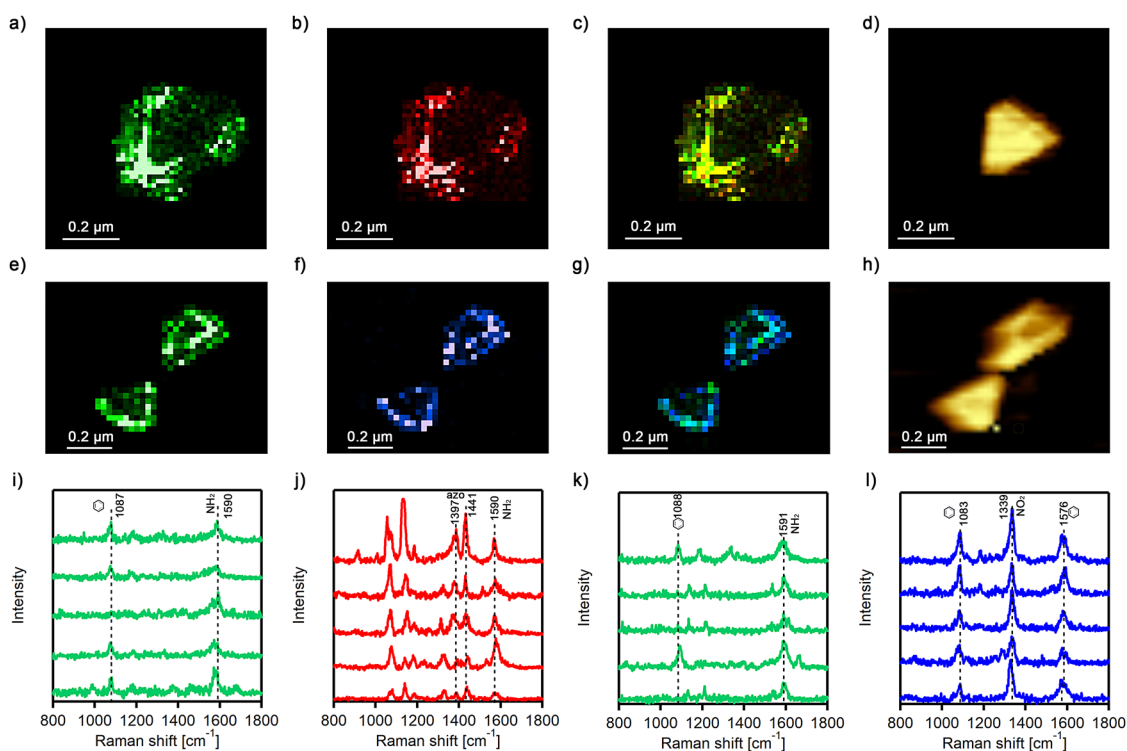

Figure 9: Photo oxidation of 4-ATP to DMAB and 4-NBT.
(a) TERS image of 4-ATP and (b) DMAB, as well as (c) TERS image of AuNPs with both NO$_2$ and N=N vibrations; (d) corresponding AFM image of AuNPs; (e) TERS image of 4-ATP on Au@PtNPs; (f) TERS image of 4-NBT on Au@PtNPs; (g) TERS image of Au@PtNPs from overlapping NH$_2$ and NO$_2$ vibrations. Intensity of 1590 cm^{-1} band (NH$_2$ vibration) of 4-ATP is shown in green; intensity of 1339 cm^{-1} band (NO$_2$ vibration) of 4-NBT is shown in blue; and intensity of 1397, 1441 cm^{-1} band (azo vibration) of DMAB is shown in red. (h) Corresponding AFM image of Au@Pt NPs; (i–j) Typical TERS spectra extracted from chemical maps on AuNPs (a–c) showing presence of 4-ATP (green) and DMAB (red). (k–l) Typical TERS spectra extracted from chemical maps on AuNPs (e–g) showing presence of 4-ATP (green) and 4-NBT (blue). The resolution of each TERS image is 20 nm per pixel, with 0.5 s acquisition time [89].
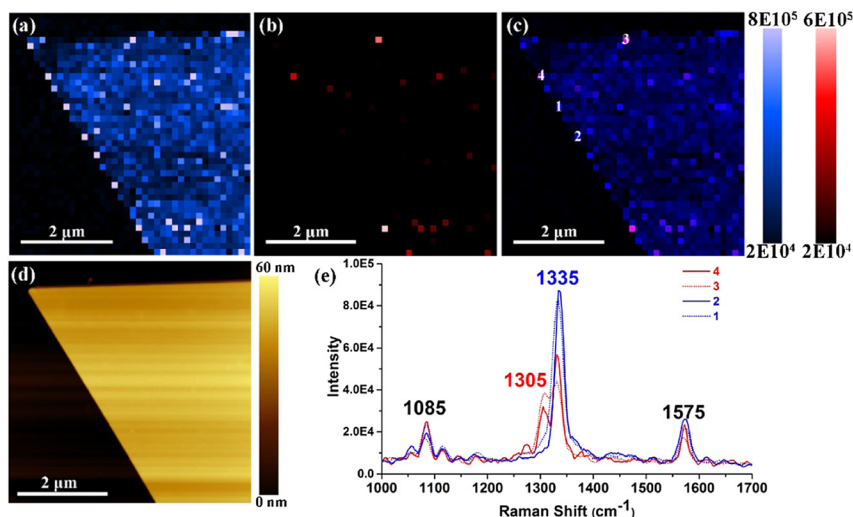
Figure 10: TER images of 4NBT monolayer on gold Au (111) surface.
(a) and (b) visual representations of integral intensities of the spectrum from 1320 to 1350 cm^{-1} (a) and 1290 to 1320 cm^{-1} (b), respectively. (c) Overlapped image of (a) and (b). (d) Corresponding AFM image of the area of TER images. (e) Typical TERS spectra extracted from the marked position in (c). The scanning step was 20 nm per pixel [26].

coauthors recently showed that lower-coordinated surface sites such as corners, edges and {100} facets exhibited a higher hot electron reactivity comparing to the higher-coordinated surface sites such as {111} facets or the core sites [97].

Wang and Kurouski recently reported a new class of plasmon-driven scissoring reactions. The researchers found that 4-NBT could be converted into 4-nitrobenzothiolate (4-NBT⁻) on the surface of AuNPs [26]. This conclusion was made by an observation of the shift of the 1335 cm^{-1} vibration of 4-NBT to the 1305 cm^{-1} vibration of 4-NBT⁻ (Figure 10). Using DFT calculations, we confirmed that this shift did not originate from electric field-induced shifts in the N–O vibrational resonance (Stark shift). An approximately 140 MV cm^{-1} field would be required to shift the N–O vibration from 1333 to 1305 cm^{-1}. Obviously, such an electric field could not be achieved in the reported TERS experiment (λ = 633 nm, P = 60 μW). We also demonstrated that the observed spectroscopic changes could not be caused by a change in molecular orientation of the analyte relative to the metal surface. It should be noted that thermal desorption of 4-NBT would require 2100 K in the tip-sample junction, which cannot be achieved in TERS [26].

Although the yield of 4-NBT ionization on AuNPs is relatively low (~1.5%) [26], the El-Khoury's group showed that AgNPs exhibited nearly 100% conversion of 4-NBT to 4-NBT⁻ [98]. Thus, the yield of the Au–S scissoring reaction is determined by the choice of the plasmonic metal. An even more fascinating discovery was uncovered with TERS imaging by comparing Ag nanotubes (AgNCs) with a monolayer of 4-NBT using the contact and tapping AFM-TERS modes [99]. Nearly all TERS spectra collected in contact mode from AgNCs showed the presence of 4-NBT⁻, whereas such 4-NBT⁻ signatures were rare in tapping mode

TERS. There are two possible explanations, based on the strength of the electric field in the tip-sample junction or quantum physics. The strength of the electric field in the Au (tip) and Au (sample) junction is lower than the strength of the electric field in an analogous Ag–Au junction [100]. This difference is attributed to different values of imaginary parts of dielectric constants of Au and Ag in the visible part of the electromagnetic spectrum. Thus, higher strength external electric fields yield more 4-NBT⁻. However, such an explanation may sound questionable because a higher electric field would yield more DMAB than 4-NBT⁻ under the same experimental conditions [90]. The second explanation considers quantum physics: quantum plasmons are exclusively responsible for molecular charging and chemical transformations observed in Au–S bonds. Thus, in tapping mode, quantum plasmons relax as the probe is distal from the surface, whereas such relaxation is not possible in the contact mode (Figure 11).
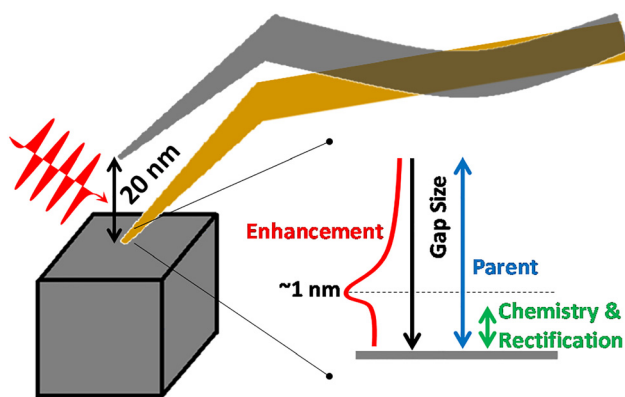

Figure 11: Local optical field properties as inferred from molecular signatures in contact versus tapping mode TERS [98].

Using ultra-high vacuum (UHV) TERS, the Ren's group investigated nanoscale activity of a submonolayer of Pd on the Au surface [101]. Using phenyl isocyanide (PIC) as a molecular reporter for TER spectra collected at Pd edges, they showed that the C≡N vibration of PIC was red-shifted by 60 cm^{-1} relative to molecules located on the Pd terrace. These results indicated that the degree of back donation from the d band of the metal to the antibonding $\pi^\star$ orbital of PIC at the step site was greater than at the terrace sites. Therefore, molecules located at Pd edges have higher reactivity than Pd atoms in terraces.

Our group utilized TERS to investigate plasmon-driven reactivity and selectivity on gold–platinum nanoplates (Au@PtNPs) [89]. These nanostructures exhibited a step-wise photo-oxidation of 4-ATP, first to 4-NBT and then to DMAB. Such selectivity was not observed using analogous monometallic structures, namely gold nanoplates (AuNPs) [26, 89, 96]. The edges of Au@PtNPs exhibited higher reactivity in plasmon-driven oxidation reactions than flat terraces. Interestingly, core–shell gold–palladium micro-plates (Au@PdMPs) supported selectivity in photoreduc-tion reactions, which was not evident for monometallic analogs (AuMPs) or core–shell Au@PtNPs [89, 90]. Specifically, Au@PdMPs photo-reduced 4-NBT to both 4-ATP and DMAB, Figure 12. This can be explained by LSPR damping in these bimetallic nanostructures due to an increased probability of interband transitions. The last can be attributed to close energy levels of d bands and Fermi levels in Pd and Pt [63].

Using TERS, Li and Kurouski measured the reaction rates for reduction of 4-NBT to DMAB on the surface of Au@PdMPs under different external electric fields. It was
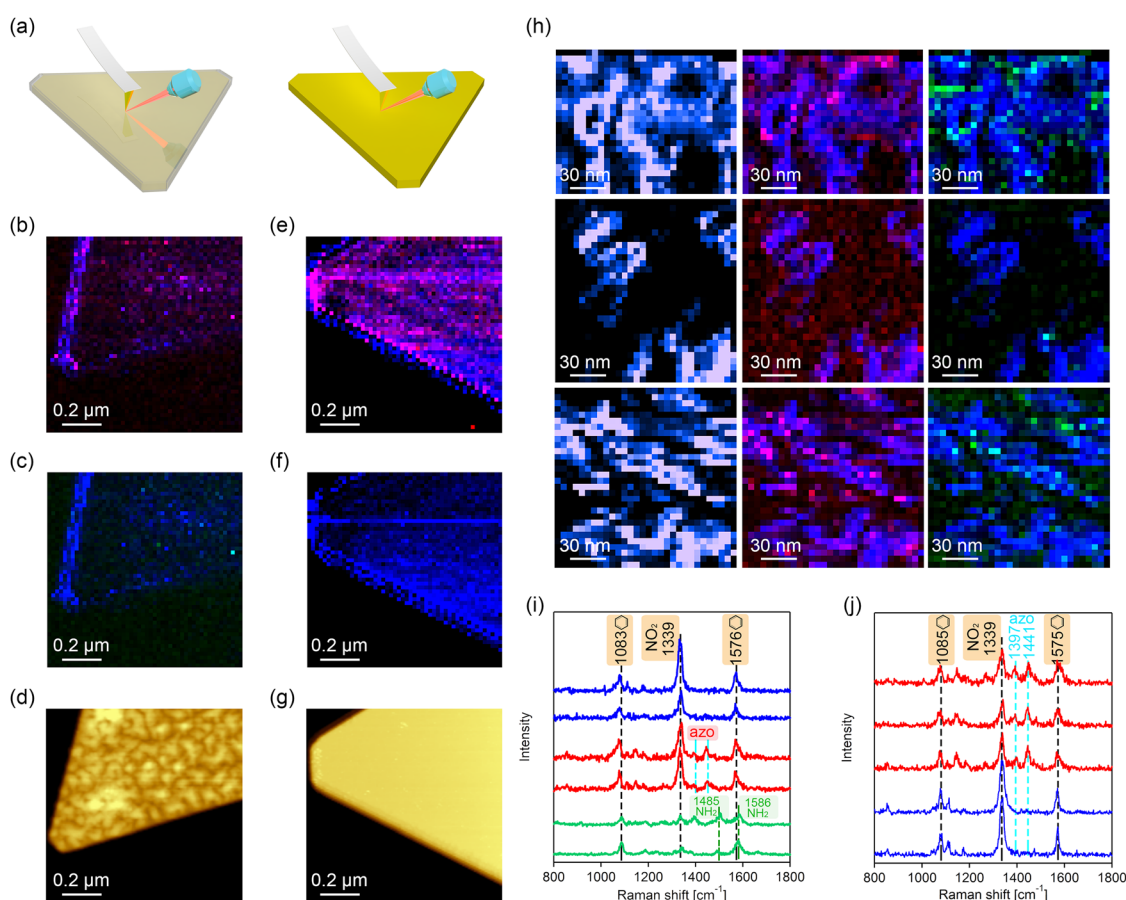

Figure 12: (a) Schematic illustration of TER imaging of Au@Pd (left) and AuMPs (right). (b–c) TERS image of Au@Pd MPs (20 nm per pixel). Intensity of 1339 cm^{-1} band (NO$_2$ vibration) of 4-NBT shown as blue, intensities of 1397 and 1451 cm^{-1} (N=N vibration) of DMAB shown as red, and intensities of 1485 cm^{-1} (NH$_2$ vibration) shown in green. (d) Corresponding AFM (bottom) images of Au@Pd MPs. (e–f) TERS image of AuMPs (20 nm per pixel). Intensity of 1338 cm^{-1} band (NO$_2$ vibration) of 4-NBT shown in blue, and intensities of 1397 and 1447 cm^{-1} (N=N vibration) of DMAB shown in red. (g) Corresponding AFM (bottom) images of AuMPs. (h) Nanoscale images (5 nm/pixel) of Au@PdMPs showing distribution of intensities of NO$_2$ vibration, left panels; overlaid NO$_2$ and N=N vibrations, center panels, and overlaid NO$_2$ and NH$_2$ vibration (1485 cm^{-1}), right panels. (i–j) Typical TERS spectra extracted from chemical maps on Au@PdMPs (b, c) and AuMPs (e, f) showing presence of 4-NBT (blue), DMAB (red) and 4-ATP (green) [90].

found that an increase in the electric field caused a linear increase in the reaction rate of 4-NBT to DMAB conversion. The researchers also found that the rates of hot-carrier driven reduction of 4-NBT to DMAB were greater on AuMPs than on Au@PdMPs. This confirms the LSPR damping hypothesis and explains the selectivity of Au@PdMPs [90].

TERS imaging of Au@PdMPs revealed spherical and rod-like patterns of Pd nanostructures on the Au surface [90]. These nanostructures showed enhanced intensity of 4-NBT relative to the underlying surface of Au@PdMPs. Li and Kurouski also determined that the edges of such spherical and rod-like Pd nanostructures exhibited high photocatalytic efficiency for 4-NBT reduction to DMAB. At the same time, "nano-lakes" between spherical nanoscale structures on the surface of Au@PdMPs showed little evidence of 4-NBT reduction. These results demonstrate charge transfer from Au to Pd on the surface of Au@PdMPs. They also suggest that Pd–Au coupling in a single nanostructure enables transfer of photocatalytic properties from noble metals to catalytic metals. Similar conclusions were independently made by the Zenobi's group [102]. They found that chloro-nitrobenzenethiol was reduced to chloro-aminobenzenethiol on an Au surface with a sub-monolayer of Pd. Yin and coworkers also demonstrated that halogenated nitrobenzenethiol was reduced to aminobenzenethiol on Au, within 20 nm of the bimetallic Pd/Au boundary.

Monometallic Pd and bimetallic Au@Pd nanostructures have unique properties to catalyze Suzuki-Miyaura coupling reactions [41]. As a result of such reactions, organoboron species and halides are cross-coupled. Using TERS, we investigated the nanoscale catalytic efficiency of Au@PdMPs for Suzuki-Miyaura coupling. The edges of Au@PdMPs exhibited a higher intensity of BPT, relative to the flat terrace. Therefore, the edges of Au@PdMPs facilitated the highest catalytic efficiency for the Suzuki-Miyaura coupling reaction. The edges of Au@PdMPs also exhibited high rates of 4-NBT reduction to DMAB and 4-ATP. Together, these results suggest that the edges of Au@PdMPs have higher catalytic activity than flat terraces.
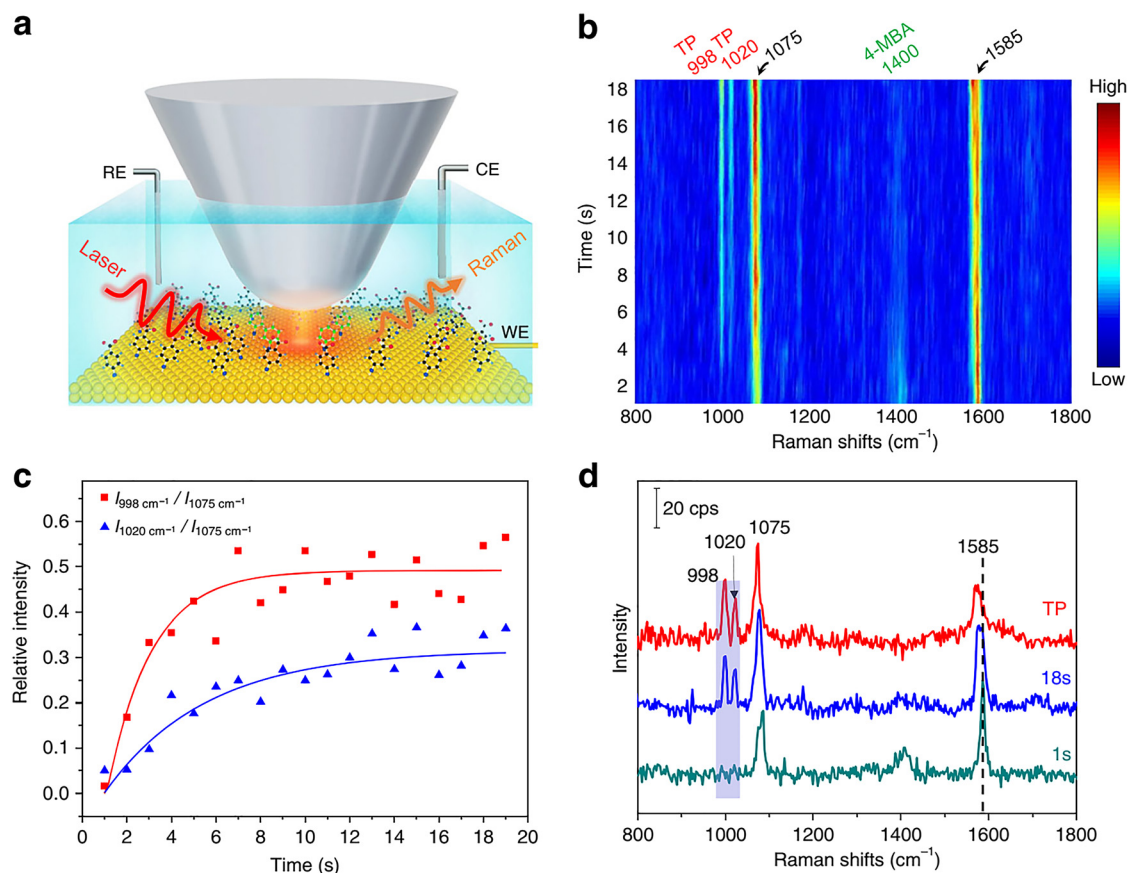

Figure 13: Decarboxylation of 4-mercaptobenzoic acid on Au (111). (a) Experimental set-up of EC-TERS where the reaction is driven under the coupled surface plasmon of silver tip and gold substrate. (b) In situ monitoring of the reaction by TERS (Power: 1.1 mW, bias: 200 mV, Itunneling: 800 pA). (c) Relative intensity of vibration bands (998 and 1020–1075 cm^{-1}) against time. (d) Representative TER spectra of 4-mercaptobenzoic acid and thiolphenol (TP) [103].
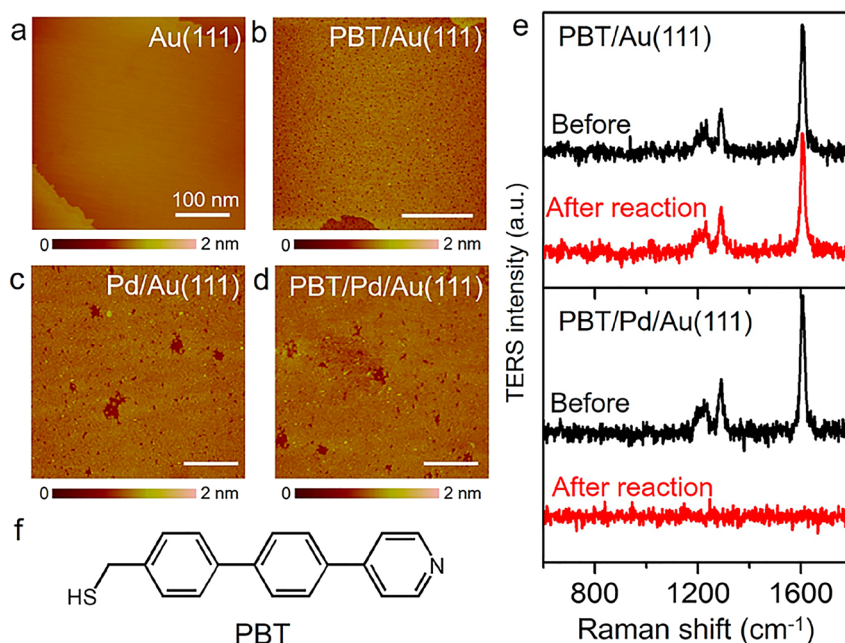
Figure 14: STM images of (a) Au (111) surface, (b) PBT/Au (111) surface, (c) Pd/Au (111) surface and (d) PBT/Pd/Au (111) surface. (e) Top: TER spectra of PBT on Au (111) surface before (black) and after (red) the treatment of 30% H_2O_2 solution. Bottom: TER spectra of PBT on Pd/Au (111) surface before (black) and after (red) the treatment of 30% H_2O_2 solution. (f) Structure of PBT molecule. All the scale bars shown are 100 nm [104].

4.3 Nanoscale analysis of plasmonic processes in electrochemical environment

Ren's group used electrochemical TERS (EC-TERS) to monitor the decarboxylation reaction on gold nanoparticles driven by surface plasmon [103]. They have shown nanoscale spatial resolution reactive hot carrier distribution at the particle surface and tuned the Fermi level of the electrode by adjusting the applied bias during TERS mapping to turn on/off the decarboxylation. The researchers have shown 20 nm of transport distance of reactive hot holes and demonstrate experimentally and theoretically that higher-energy hot holes have a shorter transport distance, Figure 13. In another study, Ren's group has shown the possibility of generation and diffusion of OH radicals on Pd/Au surface with high spatial resolution also by TERS, Figure 14 [104]. They found that the OH radicals can be catalyzed from H_2O_2 at Pd/Au (111) interfaces with the oxidation of a thiolate absorbed on the surface as a molecular reporter. They have shown TERS mapping with spatial resolution which resolve the unreacted thiolate reporter on the surface. It was found that Pd surfaces were catalytically active producing OH radicals, whereas the Pd step edges were more active than the Pd terrace while the Au surface was inactive for the generation of these radicals. Interestingly, the researchers demonstrated that the OH radicals appear at Pd step edge diffuse nearby Au and Pd

surfaces within 5.4 nm. These findings enable better understanding of the hot-carriers distribution on metal surfaces and will provide fundamental understanding of novel catalytic processes such as active oxygen species-triggered reactions.

5 Conclusion and outlook

SERS studies reported over the last decade provided an experimental evidence about the large variety of plasmon-driven chemical reactions, including C–C [46], Au-S [26], and N=N [47] cleavage, as well as reduction of 4-NBT and oxidation of 4-ATP to DMAB [34, 35, 37, 39, 40]. Although interesting from a perspective of the fundamental physics and chemistry, these findings have unclear applicability in organic and inorganic synthesis due to low reactivity and a lack of selectivity provided by noble metals. Coupling noble and catalytic metals opens an avenue for the substantial improvement in catalytic activity and selectivity [105–107]. Bimetallic catalysts also demonstrate unique catalytic activity that is not evidence for their monometallic analogs [64–66]. This allows for a substantial broadening of the spectrum of catalytic reactions and fostering green catalysis in organic and inorganic synthesis [108, 109].

Catalytic activity of bimetallic nanostructures has substantial room for improvement. This issue can be solved by labor-intense trail-and-error synthetic efforts that are used

for the optimization of catalyst activity and selectivity of bimetallic catalysts or by a tailored design of novel catalysts. The last strategy requires 1) understanding of the interplay between catalytic and noble metals; 2) elucidation of the catalytic mechanisms on solid-liquid and solid-gas interfaces and 3) determination of the relationship between the nanostructure and catalytic activity of bimetallic catalysts. High-resolution transmission electron microscopy (HR-TERS) and absorption spectroscopy are often used to obtain this information [63, 110]. However, there techniques provide only indirect evidence about catalytic activity of such catalysts.

TERS is an emerging technique that allows for direct measurements of catalytic activity and selectivity on mono and bimetallic nanostructures [91]. Nanoscale structural characterization of Au@PtNPs and Au@PdMPs by TERS revealed the relationship between a nanostructure of these novel catalysts and their catalytic activity and selectivity [89, 90]. It was found that edges and corners of both bimetallic catalysts exhibited higher activity than flat terraces. It has been also found that We found that Au@PtNPs exhibited a stepwise photo-oxidation of 4-ATP first to 4-NBT then to DMAB. Such selectivity was not observed using analogous monometallic structures. Au@PdMPs demonstrated selectivity in photo-reduction reactions, which was neither evident for their monometallic analogs nor for Au@PtNPs. Specifically, Au@PdMPs were found to photo-reduce 4-NBT to both 4-ATP and DMAB. Based on these findings, Kurouski's group concluded that catalytic activity and selectivity of bimetallic nanostructures are determined as follows: 1) nature of catalytic metals that can be described by their standard electrode potentials, 2) interplay between catalytic and noble metals at the nanoscale and 3) the strength of the electric field on the surface of catalysts [89, 90].

In the recently reported work, Li and Kurouski measured Stark shift of 4-mercaptobenzonitrile adsorbed on the surface of Au@PtNPs and Au@PdNPs to determine of the strength of the electric field on these bimetallic catalysts [111]. The researchers observed 4–6 times larger magnitudes of rectified DC field on the surface of these catalysts comparing to the electric field observed on the surface of their monometallic analogs. Moreover, Au@PtNPs and Au@PdNPs demonstrate site-specific polarity of the DC field that was not observed on AuNPs. These findings show that LSPR damping on these bimetallic nanostructures that is observed by absorption spectroscopy cannot be used directly for interpretation of catalytic activity of this novel class of catalysts. Our group also revealed the importance of an interplay between noble and catalytic metals [112]. Such interplay can be uniquely altered by thermal re-shaping of core–shell Au@PdMPs. This results in the formation of a novel class of bimetallic catalysts known as alloy nanostructures [112, 113]. TERS analysis of core–shell and alloy Au@PdMPs revealed drastic differences in catalytic activity of these bimetallic structures at the nanoscale. It should be noted that 50–60 nm thickness of these bimetallic nanostructures limit the use of HR-TEM for their structural characterization.

The use of both SERS and TERS enabled substantial progress in the understanding hot carrier-driven chemistry. Concurrently, these findings altered the perception of both techniques. Although routinely observed in SERS, plasmon-driven reactivity in the tip-sample junction was mostly ignored by the TERS community. Experimental findings discussed above, as well as recently reported results from other groups, were able to transform the perception of TERS [98, 99, 101, 114–116]. These studies triggered an interest in the use of TERS for spatiotemporal characterization of plasmon-driven reactions at the nanoscale. One can envision that this new for TERS research direction will only expand in the future.

At the same time, these findings questioned a purity of the imaging nature of TERS. C–C, N=N and other bands that can be modified by hot carriers are present in biological species, organic and inorganic polymers. One may wonder about the extent to which such bonds can be altered upon TERS imaging of these samples. This question remains unclear as two contradictory pieces of experimental evidence exist. One of them suggests about the expected chaos due to extreme complexity of possibly expected reaction products [115, 116], whereas the alternative evidence demonstrates the possibility of a clear readout of the sequence of biopolymers such as RNA and DNA [117–119] and molecular conformations on the metalized surfaces [68, 76, 82, 83, 120]. One can envision that additional experimental and theoretical studies, as well as a constructive discussion of experimental findings are required to fully understand the potential and complex nature of TERS.

References

[1] S. L. Kleinman, R. R. Frontiera, A.-I. Henry, J. A. Dieringer, and R. P. Van Duyne, "Creating, characterizing, and controlling chemistry with SERS hot spots," *Phys. Chem. Chem. Phys.*, vol. 15, no. 1, pp. 21–36, 2013.

[2] R. J. C. Brown and M. J. T. Milton, "Nanostructures and nanostructured substrates for surface-enhanced Raman scattering (SERS)," *J. Raman Spectrosc.*, vol. 39, no. 10, pp. 1313–1326, 2008.

[3] M. Moskovits, "Surface roughness and the enhanced intensity of Raman scattering by molecules adsorbed on metals," *J. Chem. Phys.*, vol. 69, no. 9, pp. 4159–4161, 1978.

[4] J. Gersten and A. Nitzan, "Electromagnetic theory of enhanced Raman scattering by molecules adsorbed on rough surfaces," *J. Chem. Phys.*, vol. 73, no. 7, pp. 3023–3037, 1980.

[5] M. Kerker, D.-S. Wang, and H. Chew, "Surface enhanced Raman scattering (SERS) by molecules adsorbed at spherical particles," *Appl. Opt.*, vol. 19, no. 19, pp. 3373–3388, 1980.

[6] F. W. King, R. P. Van Duyne, and G. C. Schatz, "Theory of Raman scattering by molecules adsorbed on electrode surfaces," *J. Chem. Phys.*, vol. 69, no. 10, pp. 4472–4481, 1978.

[7] B. Sharma, R. Frontiera, A. I. Henry, E. Ringe, and R. P. Van Duyne, "SERS: materials, applications, and the future," *Mater. Today*, vol. 15, no. 1–2, pp. 16–25, 2012.

[8] P. L. Stiles, J. A. Dieringer, N. C. Shah, and R. P. Van Duyne, "Surface-enhanced Raman spectroscopy," *Annu. Rev. Anal. Chem.*, vol. 1, no. 1, pp. 601–626, 2008.

[9] S. L. Kleinman, B. Sharma, M. G. Blaber, et al., "Structure enhancement factor relationships in single gold nanoantennas by surface-enhanced Raman excitation spectroscopy," *J. Am. Chem. Soc.*, vol. 135, no. 1, pp. 301–308, 2013.

[10] N. G. Greeneltch, M. G. Blaber, A.-I. Henry, G. C. Schatz, and R. P. Van Duyne, "Immobilized nanorod assemblies: fabrication and understanding of large area surface-enhanced Raman spectroscopy substrates," *Anal. Chem.*, vol. 85, no. 4, pp. 2297–2303, 2013.

[11] K. L. Wustholz, A.-I. Henry, J. M. McMahon, et al., "Structure–Activity relationships in gold nanoparticle dimers and trimers for surface-enhanced Raman spectroscopy," *J. Am. Chem. Soc.*, vol. 132, no. 31, pp. 10903–10910, 2010.

[12] K. L. Kelly, E. Coronado, L. L. Zhao, and G. C. Schatz, "The optical properties of metal nanoparticles: the influence of size, shape, and dielectric environment," *J. Phys. Chem. B*, vol. 107, no. 3, pp. 668–677, 2003.

[13] K. L. Wustholz, A.-I. Henry, J. M. McMahon, et al., "Structure-activity relationships in gold nanoparticle dimers and trimers for surface-enhanced Raman spectroscopy," *J. Am. Chem. Soc.*, vol. 132, no. 31, pp. 10903–10910, 2011.

[14] A. J. Haes, C. L. Haynes, A. D. McFarland, G. C. Schatz, R. P. Van Duyne, and S. Zou, "Plasmonic materials for surface-enhanced sensing and spectroscopy," *MRS Bull.*, vol. 30, no. 5, pp. 368–375, 2005.

[15] E. Ringe, J. M. McMahon, K. Sohn, et al., "Unraveling the effects of size, composition, and substrate on the localized surface plasmon resonance frequencies of gold and silver nanocubes: A systematic single-particle approach," *J. Phys. Chem. C*, vol. 114, no. 29, pp. 12511–12516, 2010.

[16] D. Kurouski, N. Large, N. Chiang, et al., "Unraveling near-field and far-field relationships for 3D SERS substrates – A combined experimental and theoretical analysis," *Analyst*, vol. 141, no. 5, pp. 1779–1788, 2016.

[17] A.-I. Henry, B. Sharma, M. F. Cardinal, D. Kurouski, and R. P. Van Duyne, "Surface-enhanced Raman spectroscopy biosensing: in vivo diagnostics and multimodal imaging," *Anal. Chem.*, vol. 88, no. 13, pp. 6638–6647, 2016.

[18] J. G. Liu, H. Zhang, S. Link, and P. Nordlander, "Relaxation of plasmon-induced hot carriers," *ACS Photonics*, vol. 5, no. 7, pp. 2584–2595, 2018.

[19] A. Manjavacas, J. G. Liu, V. Kulkarni, and P. Nordlander, "Plasmon-induced hot carriers in metallic nanoparticles," *ACS Nano*, vol. 8, no. 8, pp. 7630–7638, 2014.

[20] J. B. Khurgin, "How to deal with the loss in plasmonics and metamaterials," *Nat. Nanotechnol.*, vol. 10, no. 1, pp. 2–6, 2015.

[21] P. Narang, R. Sundararaman, and H. A. Atwater, "Plasmonic hot carrier dynamics in solid-state and chemical systems for energy conversion," *Nanophotonics*, vol. 5, no. 1, pp. 96–111, 2016.

[22] A. M. Brown, R. Sundararaman, P. Narang, W. A. Goddard, and H. A. Atwater, "Nonradiative plasmon decay and hot carrier dynamics: effects of phonons, surfaces, and geometry," *ACS Nano*, vol. 10, no. 1, pp. 957–966, 2015.

[23] G. V. Hartland, "Optical studies of dynamics in noble metal nanostructures," *Chem. Rev.*, vol. 111, no. 6, pp. 3858–3887, 2011.

[24] J. Ma, Z. Wang, and L.-W. Wang, "Interplay between plasmon and single-particle excitations in a metal nanocluster," *Nat. Commun.*, vol. 6, no. 1, pp. 1–11, 2015.

[25] E. Cortés, W. Xie, J. Cambiasso, et al., "Plasmonic hot electron transport drives nano-localized chemistry," *Nat. Commun.*, vol. 8, no. 1, pp. 1–10, 2017.

[26] R. Wang, J. Li, J. Rigor, et al., "Direct experimental evidence of hot carrier-driven chemical processes in tip-enhanced Raman spectroscopy (TERS)," *J. Phys. Chem. C*, vol. 124, no. 3, pp. 2238–2244, 2020.

[27] M. Richard-Lacroix and V. Deckert, "Direct molecular-level near-field plasmon and temperature assessment in a single plasmonic hotspot," *Light Sci. Appl.*, vol. 9, p. 35, 2020.

[28] W. Xie and S. Schlücker, "Surface-enhanced Raman spectroscopic detection of molecular chemo- and plasmo-catalysis on noble metal nanoparticles," *Chem. Commun.*, vol. 54, no. 19, pp. 2326–2336, 2018.

[29] Z. Zhang, T. Deckert-Gaudig, and V. Deckert, "Label-free monitoring of plasmonic catalysis on the nanoscale," *Analyst*, vol. 140, no. 13, pp. 4325–4335, 2015.

[30] D. Zhang, X. Wang, K. Braun et al., "Parabolic mirror-assisted tip-enhanced spectroscopic imaging for non-transparent materials," *J. Raman Spectrosc.*, vol. 40, no. 10, pp. 1371–1376, 2009.

[31] T. Hartman, C. S. Wondergem, N. Kumar, A. van den Berg, and B. M. Weckhuysen, "Surface- and tip-enhanced Raman spectroscopy in catalysis," *J. Phys. Chem. Lett.*, vol. 7, no. 8, pp. 1570–1584, 2016.

[32] S. Mukherjee, L. Zhou, A. M. Goodman et al., "Hot-electron-induced dissociation of H_2 on gold nanoparticles supported on SiO_2," *J. Am. Chem. Soc.*, vol. 136, no. 1, pp. 64–67, 2013.

[33] L. Zhou, C. Zhang, M. J. McClain, et al., "Aluminum nanocrystals as a plasmonic photocatalyst for hydrogen dissociation," *Nano Lett.*, vol. 16, no. 2, pp. 1478–1484, 2016.

[34] E. M. van Schrojenstein Lantman, T. Deckert-Gaudig, A. J. G. Mank, V. Deckert, and B. M. Weckhuysen, "Catalytic

processes monitored at the nanoscale with tip-enhanced Raman spectroscopy," *Nat. Nanotechnol.*, vol. 7, no. 9, pp. 583–586, 2012.

[35] H.-K. Choi, W.-H. Park, C.-G. Park, H.-H. Shin, K. S. Lee, and Z. H. Kim, "Metal-catalyzed chemical reaction of single molecules directly probed by vibrational spectroscopy," *J. Am. Chem. Soc.*, vol. 138, no. 13, pp. 4673–4684, 2016.

[36] H.-Y. Weng, Q.-H. Guo, X.-R. Wang, et al., "Inhibiting plasmon catalyzed conversion of para-nitrothiophenol on monolayer film of Au nanoparticles probed by surface enhanced Raman spectroscopy," *Spectrochim. Acta Mol. Biomol. Spectrosc.*, vol. 150, pp. 331–338, 2015.

[37] L. Kang, X. Han, J. Chu, et al., "In situ surface-enhanced Raman spectroscopy study of plasmon-driven catalytic reactions of 4-nitrothiophenol under a controlled atmosphere," *ChemCatChem*, vol. 7, no. 6, pp. 1004–1010, 2015.

[38] D.-Y. Wu, X.-M. Liu, Y.-F. Huang, B. Ren, X. Xu, and Z.-Q. Tian, "Surface catalytic coupling reaction of p-mercaptoaniline linking to silver nanostructures responsible for abnormal SERS enhancement: A DFT study," *J. Phys. Chem. C*, vol. 113, no. 42, pp. 18212–18222, 2009.

[39] M. Osawa, N. Matsuda, K. Yoshii, and I. Uchida, "Charge transfer resonance Raman process in surface-enhanced Raman scattering from p-aminothiophenol adsorbed on silver: Herzberg-Teller contribution," *J. Phys. Chem.*, vol. 98, no. 48, pp. 12702–12707, 1994.

[40] Y.-F. Huang, M. Zhang, L.-B. Zhao, et al., "Activation of oxygen on gold and silver nanoparticles assisted by surface plasmon resonances," *Angew. Chem. Int. Ed.*, vol. 53, no. 9, pp. 2353–2357, 2014.

[41] Y. Qi, V. Brasiliense, T. W. Ueltschi, et al., "Plasmon-driven chemistry in ferri-/ferrocyanide gold nanoparticle oligomers: A SERS study," *J. Am. Chem. Soc.*, vol. 142, no. 30, pp. 13120–13129, 2020.

[42] Y. Kim, J. G. Smith, and P. K. Jain, "Harvesting multiple electron-hole pairs generated through plasmonic excitation of Au nanoparticles," *Nat. Chem.*, vol. 10, no. 7, pp. 763–769, 2018.

[43] Y. Yu, K. D. Wijesekara, X. Xi, and K. A. Willets, "Quantifying wavelength-dependent plasmonic hot carrier energy distributions at metal/semiconductor interfaces," *ACS Nano*, vol. 13, no. 3, pp. 3629–3637, 2019.

[44] H.-S. Feng, F. Dong, H.-S. Su, M. M. Sartin, and B. Ren, "In situ investigation of hot-electron-induced Suzuki–Miyaura reaction by surface-enhanced Raman spectroscopy," *J. Appl. Phys.*, vol. 128, no. 17, p. 173105, 2020.

[45] Y. Zhao, L. Du, H. Li, W. Xie, and J. Chen, "Is the suzuki-miyaura cross-coupling reaction in the presence of Pd nanoparticles heterogeneously or homogeneously catalyzed? An interfacial surface-enhanced Raman spectroscopy study," *J. Phys. Chem. Lett.*, vol. 10, no. 6, pp. 1286–1291, 2019.

[46] H. Huh, H. D. Trinh, D. Lee, and S. Yoon, "How does a plasmon-induced hot charge carrier break a C-C bond?," *ACS Appl. Mater. Interfaces*, vol. 11, no. 27, pp. 24715–24724, 2019.

[47] M. Sun, Z. Zhang, Z. H. Kim, H. Zheng, and H. Xu, "Plasmonic scissors for molecular design," *Chem. Eur J.*, vol. 19, no. 44, pp. 14958–14962, 2013.

[48] S. Mukherjee, F. Libisch, N. Large, et al., "Hot electrons do the impossible: plasmon-induced dissociation of H2on Au," *Nano Lett.*, vol. 13, no. 1, pp. 240–247, 2013.

[49] C. Fasciani, C. J. B. Alejo, M. Grenier, J. C. Netto-Ferreira, and J. C. Scaiano, "High-temperature organic reactions at room temperature using plasmon excitation: decomposition of dicumyl peroxide," *Org. Lett.*, vol. 13, no. 2, pp. 204–207, 2011.

[50] J. Liu, Z.-Y. Cai, W.-X. Sun, et al., "Plasmonic hot electron-mediated hydrodehalogenation kinetics on nanostructured Ag electrodes," *J. Am. Chem. Soc.*, vol. 142, no. 41, pp. 17489–17498, 2020.

[51] Z. Zhang, T. Deckert-Gaudig, P. Singh, and V. Deckert, "Single molecule level plasmonic catalysis – A dilution study of p-nitrothiophenol on gold dimers," *Chem. Commun.*, vol. 51, no. 15, pp. 3069–3072, 2015.

[52] R. Schürmann and I. Bald, "Real-time monitoring of plasmon induced dissociative electron transfer to the potential DNA radiosensitizer 8-bromoadenine," *Nanoscale*, vol. 9, no. 5, pp. 1951–1955, 2017.

[53] H.-K. Choi, K. S. Lee, H.-H. Shin, J.-J. Koo, G. J. Yeon, and Z. H. Kim, "Single-molecule surface-enhanced Raman scattering as a probe of single-molecule surface reactions: promises and current challenges," *Acc. Chem. Res.*, vol. 52, no. 11, pp. 3008–3017, 2019.

[54] H.-H. Shin, J.-J. Koo, K. S. Lee, and Z. H. Kim, "Chemical reactions driven by plasmon-induced hot carriers," *Appl. Mater. Today*, vol. 16, pp. 112–119, 2019.

[55] P. Christopher, H. Xin, and S. Linic, "Visible-light-enhanced catalytic oxidation reactions on plasmonic silver nanostructures," *Nat. Chem.*, vol. 3, no. 6, pp. 467–472, 2011.

[56] S. Linic, U. Aslam, C. Boerigter, and M. Morabito, "Photochemical transformations on plasmonic metal nanoparticles," *Nat. Mater.*, vol. 14, no. 6, pp. 567–576, 2015.

[57] M. L. Brongersma, N. J. Halas, and P. Nordlander, "Plasmon-induced hot carrier science and technology," *Nat. Nanotechnol.*, vol. 10, no. 1, pp. 25–34, 2015.

[58] U. Aslam, V. G. Rao, S. Chavez, and S. Linic, "Catalytic conversion of solar to chemical energy on plasmonic metal nanostructures," *Nat. Catal.*, vol. 1, no. 9, pp. 656–665, 2018.

[59] Y. Zhang, S. He, W. Guo, et al., "Surface-plasmon-driven hot electron photochemistry," *Chem. Rev.*, vol. 118, no. 6, pp. 2927–2954, 2017.

[60] Q. Huang, T. D. Canady, R. Gupta, N. Li, S. Singamaneni, and B. T. Cunningham, "Enhanced plasmonic photocatalysis through synergistic plasmonic-photonic hybridization," *ACS Photonics*, vol. 7, no. 8, pp. 1994–2001, 2020.

[61] S. Xu, L. Guo, Q. Sun, and Z. L. Wang, "Piezotronic effect enhanced plasmonic photocatalysis by AuNPs/BaTiO 3 heterostructures," *Adv. Funct. Mater.*, vol. 29, no. 13, p. 1808737, 2019.

[62] L. Yuan, M. Lou, B. D. Clark, et al., "Morphology-Dependent reactivity of a plasmonic photocatalyst," *ACS Nano*, vol. 14, no. 9, pp. 12054–12063, 2020.

[63] K. Sytwu, M. Vadai, and J. A. Dionne, "Bimetallic nanostructures: combining plasmonic and catalytic metals for photocatalysis," *Adv. Phys. X*, vol. 4, no. 1, pp. 394–418, 2019.

[64] F. Wang, C. Li, H. Chen, et al., "Plasmonic harvesting of light energy for Suzuki coupling reactions," *J. Am. Chem. Soc.*, vol. 135, no. 15, pp. 5588–5601, 2013.

[65] L. Zhou, J. M. P. Martirez, J. Finzel, et al., "Light-driven methane dry reforming with single atomic site antenna-reactor

plasmonic photocatalysts," *Nat. Energy*, vol. 5, no. 1, pp. 61–70, 2020.

[66] Z. Lou, M. Fujitsuka, and T. Majima, "Pt-Au triangular nanoprisms with strong dipole plasmon resonance for hydrogen generation studied by single-particle spectroscopy," *ACS Nano*, vol. 10, no. 6, pp. 6299–6305, 2016.

[67] N. Jiang, E. T. Foley, J. M. Klingsporn, et al., "Observation of multiple vibrational modes in ultrahigh vacuum tip-enhanced Raman spectroscopy combined with molecular-resolution scanning tunneling microscopy," *Nano Lett.*, vol. 12, no. 10, pp. 5061–5067, 2012.

[68] J. M. Klingsporn, N. Jiang, E. A. Pozzi, et al., "Intramolecular insight into adsorbate-substrate interactions via low-temperature, ultrahigh-vacuum tip-enhanced Raman spectroscopy," *J. Am. Chem. Soc.*, vol. 136, no. 10, pp. 3881–3887, 2014.

[69] D. Kurouski, M. Mattei, and R. P. Van Duyne, "Probing redox reactions at the nanoscale with electrochemical tip-enhanced Raman spectroscopy," *Nano Lett.*, vol. 15, no. 12, pp. 7956–7962, 2015.

[70] D. Kurouski, S. Zaleski, F. Casadio, R. P. Van Duyne, and N. C. Shah, "Tip-enhanced Raman spectroscopy (TERS) for in Situ Identification of indigo and iron gall ink on paper," *J. Am. Chem. Soc.*, vol. 136, no. 24, pp. 8677–8684, 2014.

[71] D. Kurouski, "Advances of tip-enhanced Raman spectroscopy (TERS) in electrochemistry, biochemistry, and surface science," *Vib. Spectrosc.*, vol. 91, pp. 3–15, 2017.

[72] M. Richard-Lacroix, Y. Zhang, Z. Dong, and V. Deckert, "Mastering high resolution tip-enhanced Raman spectroscopy: towards a shift of perception," *Chem. Soc. Rev.*, vol. 46, no. 13, pp. 3922–3944, 2017.

[73] P. Verma, "Tip-enhanced Raman spectroscopy: technique and recent advances," *Chem. Rev.*, vol. 117, no. 9, pp. 6447–6466, 2017.

[74] M. D. Sonntag, D. Chulhai, T. Seideman, L. Jensen, and R. P. Van Duyne, "The origin of relative intensity fluctuations in single-molecule tip-enhanced Raman spectroscopy," *J. Am. Chem. Soc.*, vol. 135, no. 45, pp. 17187–17192, 2013.

[75] N. Tallarida, J. Lee, and V. A. Apkarian, "Tip-enhanced Raman spectromicroscopy on the angstrom scale: bare and CO-terminated Ag tips," *ACS Nano*, vol. 11, no. 11, pp. 11393–11401, 2017.

[76] R. Zhang, Y. Zhang, Z. C. Dong, et al., "Chemical mapping of a single molecule by plasmon-enhanced Raman scattering," *Nature*, vol. 498, no. 7452, pp. 82–86, 2013.

[77] T. Deckert-Gaudig, D. Kurouski, M. A. B. Hedegaard, P. Singh, I. K. Lednev, and V. Deckert, "Spatially resolved spectroscopic differentiation of hydrophilic and hydrophobic domains on individual insulin amyloid fibrils," *Sci. Rep.*, vol. 6, p. 33575, 2016.

[78] A. V. Krasnoslobodtsev, T. Deckert-Gaudig, Y. Zhang, V. Deckert, and Y. L. Lyubchenko, "Polymorphism of amyloid fibrils formed by a peptide from the yeast prion protein Sup35: AFM and Tip-Enhanced Raman Scattering studies," *Ultramicroscopy*, vol. 165, pp. 26–33, 2016.

[79] D. Kurouski, T. Deckert-Gaudig, V. Deckert, and I. K. Lednev, "Structure and composition of insulin fibril surfaces probed by TERS," *J. Am. Chem. Soc.*, vol. 134, no. 32, pp. 13323–13329, 2012.

[80] R. Böhme, M. Mkandawire, U. Krause-Buchholz, et al., "Characterizing cytochrome c states – TERS studies of whole mitochondria," *Chem. Commun.*, vol. 47, no. 41, pp. 11453–11455, 2011.

[81] M. Tabatabaei, F. A. Caetano, F. Pashee, S. S. G. Ferguson, and F. Lagugné-Labarthet, "Tip-enhanced Raman spectroscopy of amyloid β at neuronal spines," *Analyst*, vol. 142, no. 23, pp. 4415–4421, 2017.

[82] S. Mahapatra, Y. Ning, J. F. Schultz, L. Li, J.-L. Zhang, and N. Jiang, "Angstrom scale chemical analysis of metal supported trans- and cis-regioisomers by ultrahigh vacuum tip-enhanced Raman mapping," *Nano Lett.*, vol. 19, no. 5, pp. 3267–3272, 2019.

[83] S. Mahapatra, J. F. Schultz, Y. Ning, J.-L. Zhang, and N. Jiang, "Probing surface mediated configurations of nonplanar regioisomeric adsorbates using ultrahigh vacuum tip-enhanced Raman spectroscopy," *Nanoscale*, vol. 11, no. 42, pp. 19877–19883, 2019.

[84] T. Touzalin, A. L. Dauphin, S. Joiret, I. T. Lucas, and E. Maisonhaute, "Tip enhanced Raman spectroscopy imaging of opaque samples in organic liquid," *Phys. Chem. Chem. Phys.*, vol. 18, no. 23, pp. 15510–15513, 2016.

[85] T. Touzalin, S. Joiret, I. T. Lucas, and E. Maisonhaute, "Electrochemical tip-enhanced Raman spectroscopy imaging with 8 nm lateral resolution," *Electrochem. Commun.*, vol. 108, p. 106557, 2019.

[86] G. Kang, M. Yang, M. S. Mattei, G. C. Schatz, and R. P. Van Duyne, "In situ nanoscale redox mapping using tip-enhanced Raman spectroscopy," *Nano Lett.*, vol. 19, no. 3, pp. 2106–2113, 2019.

[87] N. Martín Sabanés, L. M. A. Driessen, and K. F. Domke, "Versatile side-illumination geometry for tip-enhanced Raman spectroscopy at solid/liquid interfaces," *Anal. Chem.*, vol. 88, no. 14, pp. 7108–7114, 2016.

[88] Z.-C. Zeng, S.-C. Huang, D.-Y. Wu, et al., "Electrochemical tip-enhanced Raman spectroscopy," *J. Am. Chem. Soc.*, vol. 137, no. 37, pp. 11928–11931, 2015.

[89] Z. Li and D. Kurouski, "Elucidation of photocatalytic properties of gold-platinum bimetallic nanoplates using tip-enhanced Raman spectroscopy," *J. Phys. Chem. C*, vol. 124, no. 23, pp. 12850–12854, 2020.

[90] Z. Li, R. Wang, and D. Kurouski, "Nanoscale photocatalytic activity of gold and gold-palladium nanostructures revealed by tip-enhanced Raman spectroscopy," *J. Phys. Chem. Lett.*, vol. 11, no. 14, pp. 5531–5537, 2020.

[91] D. Kurouski, A. Dazzi, R. Zenobi, and A. Centrone, "Infrared and Raman chemical imaging and spectroscopy at the nanoscale," *Chem. Soc. Rev.*, vol. 49, no. 11, p. 3315, 2020.

[92] A. Bhattarai, K. T. Crampton, A. G. Joly, L. Kovarik, W. P. Hess, and P. Z. El-Khoury, "Imaging the optical fields of functionalized silver nanowires through molecular TERS," *J. Phys. Chem. Lett.*, vol. 9, no. 24, pp. 7105–7109, 2018.

[93] A. Bhattarai, I. V. Novikova, and P. Z. El-Khoury, "Tip-enhanced Raman nanographs of plasmonic silver nanoparticles," *J. Phys. Chem. C*, vol. 123, no. 45, pp. 27765–27769, 2019.

[94] A. D. Mayevsky and A. M. Funston, "Control of electric field localization by three-dimensional bowtie nanoantennae," *J. Phys. Chem. C*, vol. 122, no. 31, pp. 18012–18020, 2018.

[95] H. Yang, E. O. Owiti, X. Jiang, S. Li, P. Liu, and X. Sun, "Localized surface plasmon resonance dependence on misaligned

truncated Ag nanoprism dimer," *Nanoscale Res. Lett.*, vol. 12, no. 1, pp. 1–6, 2017.

[96] R. Wang and D. Kurouski, "Elucidation of tip-broadening effect in tip-enhanced Raman spectroscopy (TERS): A cause of artifacts or potential for 3D TERS," *J. Phys. Chem. C*, vol. 122, no. 42, pp. 24334–24340, 2018.

[97] T. P. Rossi, P. Erhart, and M. Kuisma, "Hot-carrier generation in plasmonic nanoparticles: the importance of atomic structure," *ACS Nano*, vol. 14, no. 8, pp. 9963–9971, 2020.

[98] C.-F. Wang, B. T. O'Callahan, D. Kurouski, A. Krayev, and P. Z. El-Khoury, "The prevalence of anions at plasmonic nanojunctions: A closer look at p-nitrothiophenol," *J. Phys. Chem. Lett.*, vol. 11, no. 10, pp. 3809–3814, 2020.

[99] C.-F. Wang, B. T. O'Callahan, D. Kurouski, A. Krayev, Z. D. Schultz, and P. Z. El-Khoury, "Suppressing molecular charging, nanochemistry, and optical rectification in the tip-enhanced Raman geometry," *J. Phys. Chem. Lett.*, vol. 11, no. 15, pp. 5890–5895, 2020.

[100] J. Stadler, B. Oswald, T. Schmid, and R. Zenobi, "Characterizing unusual metal substrates for gap-mode tip-enhanced Raman spectroscopy," *J. Raman Spectrosc.*, vol. 44, no. 2, pp. 227–233, 2012.

[101] J.-H. Zhong, X. Jin, L. Meng, et al., "Probing the electronic and catalytic properties of a bimetallic surface with 3 nm resolution," *Nat. Nanotechnol.*, vol. 12, no. 2, pp. 132–136, 2017.

[102] H. Yin, L.-Q. Zheng, W. Fang, et al., "Nanometre-scale spectroscopic visualization of catalytic sites during a hydrogenation reaction on a Pd/Au bimetallic catalyst," *Nat. Catal.*, vol. 3, no. 10, pp. 834–842, 2020.

[103] S.-C. Huang, X. Wang, Q.-Q. Zhao, et al., "Probing nanoscale spatial distribution of plasmonically excited hot carriers," *Nat. Commun.*, vol. 11, no. 1, pp. 1–8, 2020.

[104] H.-S. Su, H.-S. Feng, Q.-Q. Zhao, et al., "Probing the local generation and diffusion of active oxygen species on a Pd/Au bimetallic surface by tip-enhanced Raman spectroscopy," *J. Am. Chem. Soc.*, vol. 142, no. 3, pp. 1341–1347, 2020.

[105] T. Chen and V. O. Rodionov, "Controllable catalysis with nanoparticles: bimetallic alloy systems and surface adsorbates," *ACS Catal.*, vol. 6, no. 6, pp. 4025–4033, 2016.

[106] M. Sankar, N. Dimitratos, P. J. Miedziak, P. P. Wells, C. J. Kiely, and G. J. Hutchings, "Designing bimetallic catalysts for a green and sustainable future," *Chem. Soc. Rev.*, vol. 41, no. 24, pp. 8099–8139, 2012.

[107] P. Bhol, M. B. Bhavya, S. Swain, M. Saxena, and A. K. Samal, "Modern chemical routes for the controlled synthesis of anisotropic bimetallic nanostructures and their application in catalysis," *Front. Chem.*, vol. 8, p. 357, 2020.

[108] T.-W. Zhang, *Bimetallic Nanostructures: Shape-Controlled Synthesis for Catalysis, Plasmonics, and Sensing Applications*, New York, Whiley, 2018.

[109] K. D. Gilroy, A. Ruditskiy, H.-C. Peng, D. Qin, and Y. Xia, "Bimetallic nanocrystals: syntheses, properties, and applications," *Chem. Rev.*, vol. 116, no. 18, pp. 10414–10472, 2016.

[110] A. Joplin, S. A. Hosseini Jebeli, E. Sung, et al., "Correlated absorption and scattering spectroscopy of individual platinum-decorated gold nanorods reveals strong excitation enhancement in the nonplasmonic metal," *ACS Nano*, vol. 11, no. 12, pp. 12346–12357, 2017.

[111] Z. Li, J. Rigor, N. Large, P. Z. El-Khoury, and D. Kurouski, "Underlying mechanisms of hot carrier-driven reactivity on bimetallic nanostructures," *J. Phys. Chem. C*, vol. 125, no. 4, pp. 2492–2501, 2021.

[112] Z. Li, P. Z. El-Khoury and D. Kurouski, "Tip-enhanced Raman imaging of photocatalytic reactions on thermally-reshaped gold and gold-palladium microplates," *Chem. Commun.*, vol. 57, no. 7, p. 891, 2021.

[113] R. Wang and D. Kurouski, "Thermal reshaping of gold microplates: three possible routes and their transformation mechanisms," *ACS Appl. Mater. Interfaces*, vol. 11, no. 44, pp. 41813–41820, 2019.

[114] P. Singh, T. Deckert-Gaudig, Z. Zhang, and V. Deckert, "Plasmon induced deprotonation of 2-mercaptopyridine," *Analyst*, vol. 145, no. 6, pp. 2106–2110, 2020.

[115] J. Szczerbinski, L. Gyr, J. Kaeslin, and R. Zenobi, "Plasmon-driven photocatalysis leads to products known from E-beam and X-ray-induced surface chemistry," *Nano Lett.*, vol. 18, no. 11, pp. 6740–6749, 2018.

[116] J. Szczerbinski, J. B. Metternich, G. Goubert, and R. Zenobi, "How peptides dissociate in plasmonic hot spots," *Small*, vol. 16, no. 4, p. 1905197, 2020.

[117] X.-M. Lin, T. D. Gaudig, P. Singh, and M. Siegmann, "Direct base-to-base transitions in ssDNA revealed by tip-enhanced Raman scattering," arXiv:1604.06598, 2016.

[118] R. Treffer and V. Deckert, "Recent advances in single-molecule sequencing," *Curr. Opin. Biotechnol.*, vol. 21, no. 1, pp. 4–11, 2010.

[119] R. Treffer, X. Lin, E. Bailo, T. Deckert-Gaudig, and V. Deckert, "Distinction of nucleobases – A tip-enhanced Raman approach," *Beilstein J. Nanotechnol.*, vol. 2, no. 1, pp. 628–637, 2011.

[120] J. M. Marr and Z. D. Schultz, "Imaging electric fields in SERS and TERS using the vibrational Stark effect," *J. Phys. Chem. Lett.*, vol. 4, no. 19, 2013.